The Abdus Salam
International Centre for Theoretical Physics

United Nations
Educational, Scientific and
Cultural Organization

IAEA
International Atomic Energy Agency

2354-20

Summer School on Cosmology

16 - 27 July 2012

The Cosmic Microwave Background - Slides

R. Durrer
Geneva University

Strada Costiera 11, 34151 Trieste, Italy - Tel.+39 040 2240 111; Fax +39 040 224 163 - sci_info@ictp.it

The Cosmic Microwave Background

Ruth Durrer
Université de Genève
Départment de Physique Théorique et Center for Astroparticle Physics

ICTP Summer School on Cosmology, Trieste, July 2012

Outline

Literature:
Ruth Durrer, ”The Cosmic Microwave Background”, Cambridge 2008

Angular diameter distance

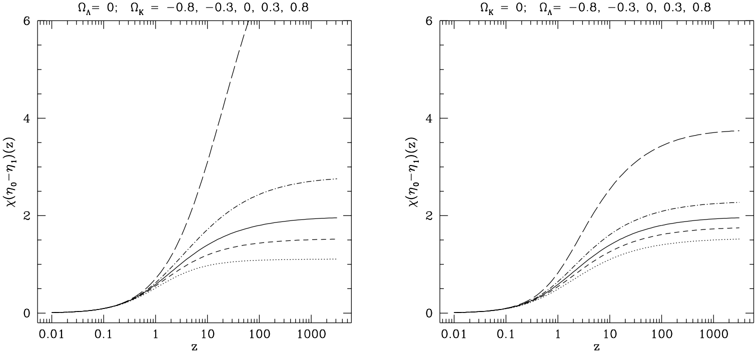

Left: $\Omega_\Lambda = 0$, $\Omega_K =$ -0.8 (dotted), -0.3 (short dashed), 0 (solid), 0.3 (dot-dashed), 0.8 (long dashed)
Right: $\Omega_K = 0$, $\Omega_\Lambda =$ -0.8 (dotted), -0.3 (short dashed), 0 (solid), 0.3 (dot-dashed), 0.8 (long dashed)

Supernovae 1a

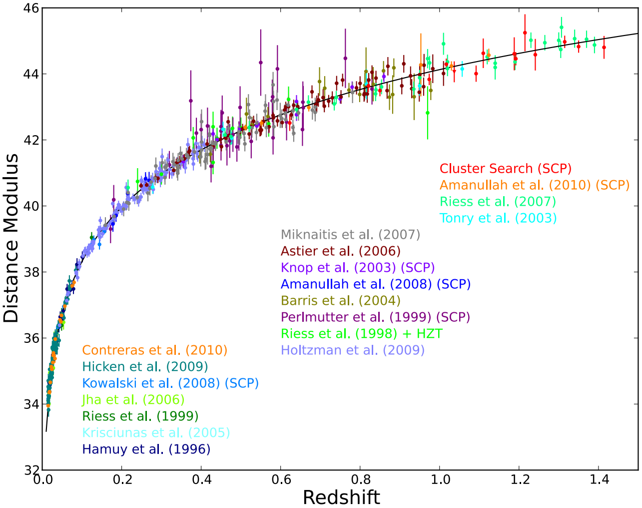

The Union2.1 data-set of SN1A's (Suzuki et al '11).

Supernovae 1a

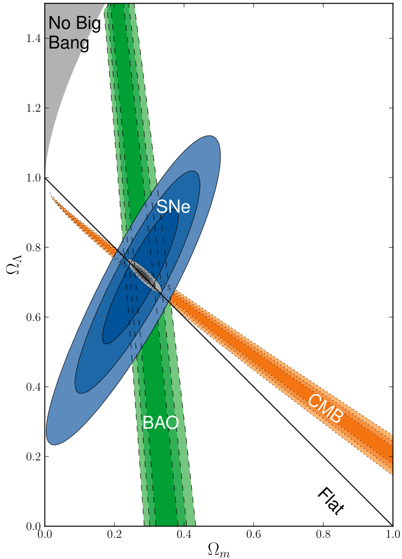

(Suzuki et al '11)

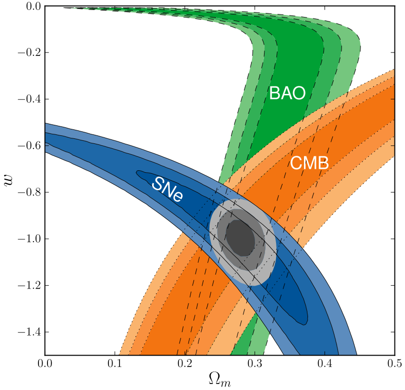

Cosmological parameters Ω_m and Ω_Λ

Ω_m and w of dark energy.

CMB radiation spectrum

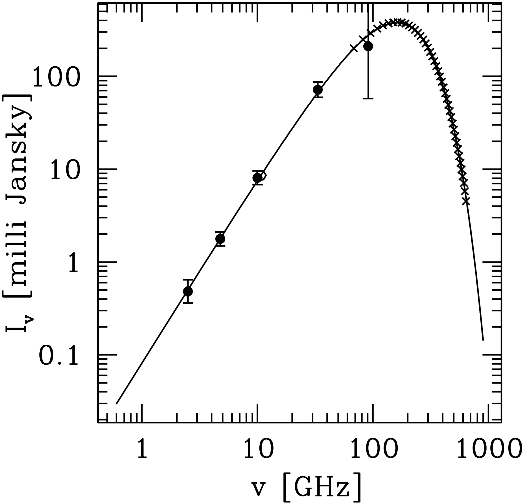

Line = blackbody at $T = 2.728$K (10GHz $= (3\mathrm{cm})^{-1}$).

Density perturbation spectrum

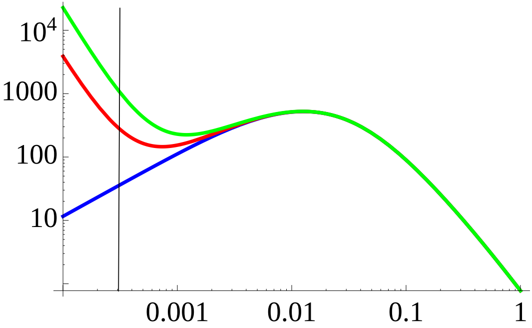

Comparing density fluctuation spectra as function of k [h/Mpc] in different gauges: comoving gauge (blue), longitudinal gauge (red) and spatially flat gauge (green)

The constraints

$$\left.\begin{array}{rcll} 4\pi G a^2 \rho D &=& -(k^2-3K)\Phi & (00) \\ 4\pi G a^2(\rho+P)V &=& k\left(\mathcal{H}\Psi+\dot\Phi\right) & (0i) \end{array}\right\} \qquad \text{(scalar)}$$

$$8\pi G a^2(\rho+P)\Omega = \frac{1}{2}\left(2K-k^2\right)\sigma^{(V)} \quad (0i) \qquad \text{(vector)}\ .$$

The dynamical equations

$$\begin{array}{lrcll} \text{scalar :} & k^2\left(\Phi-\Psi\right) &=& 8\pi G a^2 P\Pi^{(S)} & (i\neq j) \\ & \ddot\Phi+2\mathcal{H}\dot\Phi+\mathcal{H}\dot\Psi+\left[2\dot{\mathcal{H}}+\mathcal{H}^2-\frac{k^2}{3}\right]\Psi &=& 4\pi G a^2\rho\left[\frac{1}{3}D+c_s^2 D_s+w\Gamma\right] & (ii) \\ \text{vector :} & k\left(\dot\sigma^{(V)}+2\mathcal{H}\sigma^{(V)}\right) &=& 8\pi G a^2 P\Pi^{(V)} & \\ \text{tensor :} & \ddot H^{(T)}+2\mathcal{H}\dot H^{(T)}+\left(2K+k^2\right)H^{(T)} &=& 8\pi G a^2 P\Pi^{(T)}\ . & \end{array}$$

Energy momentum conservation

$$\left.\begin{array}{c}\dot{D}_g + 3\left(c_s^2 - w\right)\mathcal{H}D_g + (1+w)kV + 3w\mathcal{H}\Gamma = 0 \\ \dot{V} + \mathcal{H}\left(1-3c_s^2\right)V = k\left(\Psi + 3c_s^2\Phi\right) + \frac{c_s^2 k}{1+w}D_g \\ \qquad + \frac{wk}{1+w}\left[\Gamma - \frac{2}{3}\left(1-\frac{3K}{k^2}\right)\Pi\right]\end{array}\right\} \qquad \text{(scalar)}$$

$$\dot{\Omega} + \left(1-3c_s^2\right)\mathcal{H}\Omega = -\frac{w}{2(1+w)}\left(k - \frac{2K}{k}\right)\Pi^{(V)} \qquad \text{(vector)}\ .$$

The Bardeen equation

$$\ddot{\Psi} + 3\mathcal{H}(1+c_s^2)\dot{\Psi} + \left[3(c_s^2-w)\mathcal{H}^2 - (2+3w+3c_s^2)K + c_s^2k^2\right]\Psi$$
$$= 8\pi Ga^2P\left[\mathcal{H}\dot{\Pi} + [2\dot{\mathcal{H}} + 3\mathcal{H}^2(1-c_s^2/w)]\Pi - \frac{1}{2}k^2\Pi + \frac{1}{2}\Gamma\right].$$

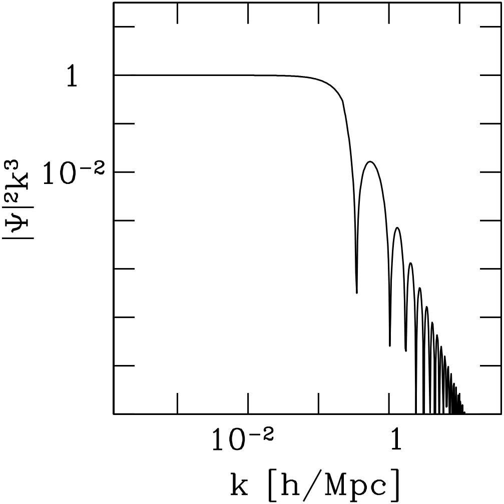

Sketch of the Bardeen potential in the matter dominated era.

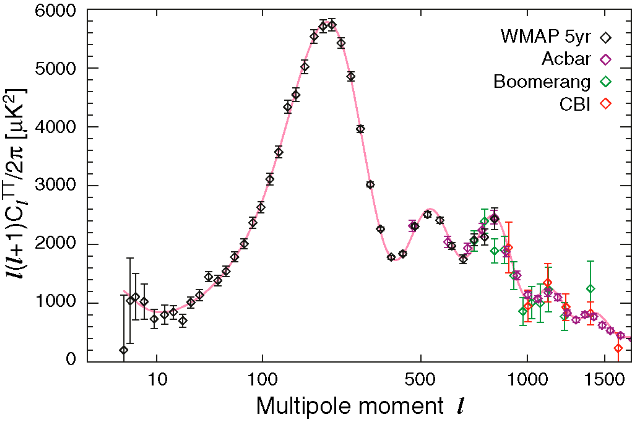

Caclulated and measured CMB anisotropies

$$F = \bar{f}(v) + F(t, \mathbf{x}, v, \mathbf{n}) \;, \qquad \mathcal{F} = F + \Phi v \frac{d\bar{f}}{dv} \;.$$

For massless particles, no collisions

$$(\partial_0 + n^i \partial_i)\mathcal{F} = n^i \partial_i (\Phi + \Psi) v \frac{d\bar{f}}{dv}$$

$$(\partial_0 + n^i \partial_i)\mathcal{M} = -n^i \partial_i (\Phi + \Psi) \;, \qquad \mathcal{M} = \frac{\pi}{a^4 \bar{\rho}} \int v^3 \mathcal{F} dv$$

Integral solution:

$$\begin{aligned} \mathcal{M}(t, \mathbf{x}, \mathbf{n}) &= \mathcal{M}(t_i, \mathbf{x} - \mathbf{n}(t - t_i), \mathbf{n}) - \int_{t_i}^{t} dt' n^i \partial_i (\Phi + \Psi)(t', \mathbf{x} - \mathbf{n}(t - t')) \\ &= \mathcal{M}(t_i, \mathbf{x}_i, \mathbf{n}) - (\Phi + \Psi)(t, \mathbf{x}_i) + \int_{t_i}^{t} dt' \partial_{t'} (\Phi + \Psi)(t', \mathbf{x}(t')) \end{aligned}$$

In Fourier space: $\mathcal{M}(t, \mathbf{k}, \mathbf{n}) = \sum_{\ell} (-i)^{\ell} (2\ell + 1) P_{\ell}(\mu) \mathcal{M}_{\ell}(\mathbf{k}, t)$

$$\partial_t \mathcal{M}_{\ell} + k \frac{\ell + 1}{2\ell + 1} \mathcal{M}_{\ell+1} - k \frac{\ell}{2\ell + 1} \mathcal{M}_{\ell-1} = \frac{1}{3} \delta_{\ell 1} k (\Phi + \Psi) \;.$$

Boltzmann equation

Collision term

$$C[\mathcal{F}] = \frac{df_+}{dt} - \frac{df_-}{dt} = a\sigma_T n_e \left[\frac{1}{4}D_g^{(r)} - \mathcal{M} - n^i V_i^{(b)} + \frac{1}{2}n_{ij}M^{ij}\right], M^{ij} \equiv \frac{3}{8\pi}\int n_{ij}\mathcal{M}(\mathbf{n})d\Omega_{\mathbf{n}}$$

$$n_{ij} = n_i n_j - \frac{1}{3}\delta_{ij}\,, \quad a\sigma_T n_e = \dot{\kappa}$$

$$(\partial_t + ik\mu)\mathcal{M} = ik\mu(\Phi+\Psi) + \dot{\kappa}\left[\frac{1}{4}D_g^{(r)} - \mathcal{M} - i\mu V^{(b)} - \frac{1}{2}\mathcal{M}_2 P_2(\mu)\right]$$

Integral solution

$$\mathcal{M}(t_0, \mathbf{k}, \mu) = \int_0^{t_0} dt e^{ik\mu(t-t_0)} S(t, \mathbf{k})\,, \quad \text{with}$$

$$S = -e^{-\kappa}(\dot{\Phi}+\dot{\Psi}) + g\left(\Phi + \Psi + k^{-1}\dot{V}^{(b)} + \frac{1}{4}D_g^{(r)} + \frac{1}{4}\mathcal{M}_2\right) + k^{-1}\dot{g}V^{(b)} - \frac{3}{4k^2}\frac{d^2}{dt^2}(g\mathcal{M}_2)$$

$g = \dot{\kappa}e^{-\kappa}$ is the visibility function.

$$\mathcal{M}_\ell(t_0, \mathbf{k}) = \int_0^{t_0} dt j_\ell(k(t_0 - t))S(t, \mathbf{k})$$

$$\langle \mathcal{M}_\ell(t_0, \mathbf{k}')\mathcal{M}^*_{\ell'}(t_0, \mathbf{k}')\rangle = (2\pi)^3\delta(\mathbf{k}.\mathbf{k}')\delta_{\ell\ell'}M_\ell(k)\,, \qquad C_\ell = \frac{2}{\pi}\int\frac{dk}{k}k^3 M_\ell(k)$$

Optical depth and visibility function

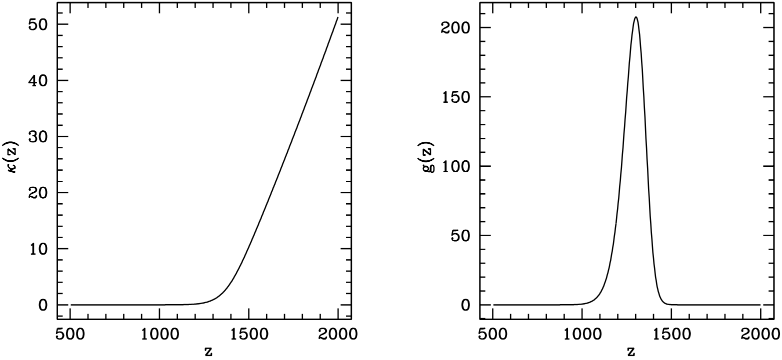

The optical depth κ (left) and the visibility function g (right).

Polarization

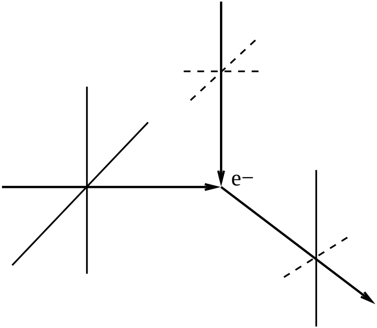

A quadrupole anisotropy on the last scattering surface induces polarisation.

E- and B-polarization

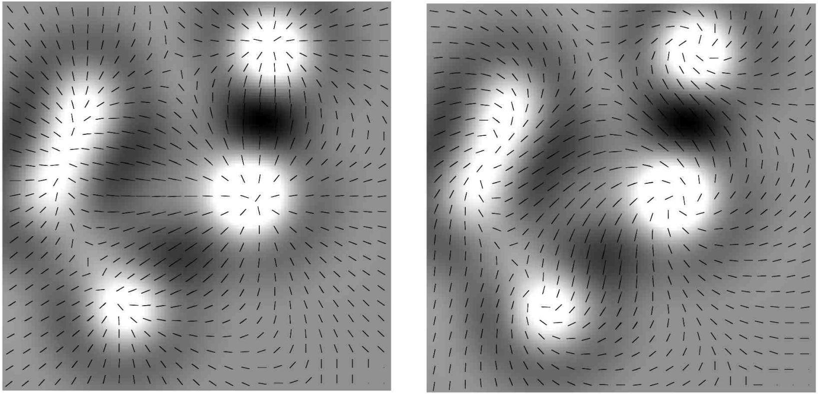

A E-polarization pattern (left) is compared with B-polarization. The function $\tilde{\mathcal{E}} = \tilde{\mathcal{B}}$ is indicated in grey scale, and the polarization directions are drawn. E-polarization is tangential along the dark negative regions while it is radial from the white white positive regions. The B-polarization pattern ban be obtained by rotating the polarization directions by 45^o.

Scattering

$$
\begin{aligned}
(\partial_t + n^i\partial_i)\mathcal{V} &= C[\mathcal{V}] + \begin{pmatrix} S \\ 0 \\ 0 \end{pmatrix}, \qquad \mathcal{V} = \begin{pmatrix} \mathcal{M} \\ \mathcal{Q} + i\mathcal{U} \\ \mathcal{Q} - i\mathcal{U} \end{pmatrix} \\
C[\mathcal{V}] &= \dot\kappa \left[\frac{1}{10} \int \Omega_{\mathbf{n}'} \sum_{m=-2}^{2} P_m(\mathbf{n},\mathbf{n}')\mathcal{V}(\mathbf{n}') - \mathcal{V}(\mathbf{n}) \right. \\
&\qquad \left. + \left[\frac{1}{4\pi} \int \Omega_{\mathbf{n}'} \mathcal{M}(\mathbf{n}') + \mathbf{n}\cdot\mathbf{V}^{(b)} \right] \begin{pmatrix} 1 \\ 0 \\ 0 \end{pmatrix} \right].
\end{aligned}
$$

$$
P_m(\mathbf{n},\mathbf{n}') = \begin{pmatrix}
Y_{2m}(\mathbf{n})Y^*_{2m}(\mathbf{n}') & -\sqrt{\frac{3}{2}}\,Y_{2m}(\mathbf{n})\,{}_2Y^*_{2m}(\mathbf{n}') & -\sqrt{\frac{3}{2}}\,Y_{2m}(\mathbf{n})\,{}_{-2}Y^*_{2m}(\mathbf{n}') \\
-\sqrt{6}\,{}_2Y_{2m}(\mathbf{n})Y^*_{2m}(\mathbf{n}') & 3\,{}_2Y_{2m}(\mathbf{n})\,{}_2Y^*_{2m}(\mathbf{n}') & 3\,{}_2Y_{2m}(\mathbf{n})\,{}_{-2}Y^*_{2m}(\mathbf{n}') \\
-\sqrt{6}\,{}_{-2}Y_{2m}(\mathbf{n})Y^*_{2m}(\mathbf{n}') & 3\,{}_{-2}Y_{2m}(\mathbf{n})\,{}_2Y^*_{2m}(\mathbf{n}') & 3\,{}_{-2}Y_{2m}(\mathbf{n})\,{}_{-2}Y^*_{2m}(\mathbf{n}')
\end{pmatrix}
$$

Total angular momentum method

$$ {}_sG_{\ell m}(\mathbf{x},\mathbf{n}) = (-i)^\ell \sqrt{\frac{4\pi}{2\ell+1}} e^{i\mathbf{k}\cdot\mathbf{x}} {}_sY_{\ell m}(\mathbf{n}) $$

$$ \begin{aligned} \mathcal{M}(t,\mathbf{x},\mathbf{n}) &= \int \frac{d^3k}{(2\pi)^3} \sum_{\ell=0}^{\infty} \sum_{m=-2}^{2} \mathcal{M}_\ell^{(m)}(t,\mathbf{k}) {}_0G_{\ell m}(\mathbf{x},\mathbf{n}) \\ \mathcal{Q} \pm i\mathcal{U} &= \int \frac{d^3k}{(2\pi)^3} \sum_{\ell=2}^{\infty} \sum_{m=-2}^{2} \left(\mathcal{E}_\ell^{(m)}(t,\mathbf{k}) \pm i\mathcal{B}_\ell^{(m)}(t,\mathbf{k})\right) {}_{\pm 2}G_{\ell m}(\mathbf{x},\mathbf{n}) . \end{aligned} $$

$$ {}_sG_{\ell m}(-r\mathbf{n},\mathbf{n}) = \sum_{j=0}^{\infty} (-i)^j \sqrt{4\pi(2j+1)}\, {}_sf_j^{(\ell m)}(kr)\, {}_sY_{jm}(\mathbf{n}) . $$

$$ {}_sf_j^{(\ell m)}(x) \equiv \sum_{L=|j-\ell|}^{j+\ell} (-i)^{L+\ell-j} \frac{2L+1}{2j+1} \langle L,\ell;0,m|j,m\rangle \langle L,\ell;0,-s|j,-s\rangle j_L(x) $$

$$ \alpha_j^{(\ell m)} \equiv {}_0f_j^{(\ell m)} $$

$$ \epsilon_j^{(\ell m)} \pm i\beta_j^{(\ell m)} \equiv {}_{\pm 2}f_j^{(\ell m)} $$

Total angular momentum method

$$
\begin{aligned}
\alpha_\ell^{(00)}(x) &= j_\ell(x) \\
\alpha_\ell^{(10)}(x) &= j'_\ell(x)\,, \quad \alpha_\ell^{(1\,\pm1)}(x) = \sqrt{\frac{\ell(\ell+1)}{2}}\frac{j_\ell(x)}{x} \\
\alpha_\ell^{(20)}(x) &= \frac{1}{2}[3j''_\ell(x) + j_\ell(x)], \quad \alpha_\ell^{(2\,\pm1)}(x) = \sqrt{\frac{3\ell(\ell+1)}{2}}\left(\frac{j_\ell(x)}{x}\right)' \\
\alpha_\ell^{(2\,\pm2)}(x) &= \sqrt{\frac{3(\ell+2)!}{8(\ell-2)!}}\frac{j_\ell(x)}{x^2} = \epsilon_\ell^{(20)}(x) \\
\epsilon_\ell^{(2\,\pm1)}(x) &= \frac{1}{2}\sqrt{(\ell-1)(\ell+2)}\left[\frac{j_\ell(x)}{x^2} + \frac{j'_\ell(x)}{x}\right] \\
\epsilon_\ell^{(2\,\pm2)}(x) &= \frac{1}{4}\left[-j_\ell(x) + j''_\ell(x) + 2\frac{j_\ell(x)}{x^2} + 4\frac{j'_\ell(x)}{x}\right], \\
\beta_\ell^{(20)}(x) &= 0 \\
\beta_\ell^{(2\,\pm1)}(x) &= \pm\frac{1}{2}\sqrt{(\ell-1)(\ell+2)}\frac{j_\ell(x)}{x} \\
\beta_\ell^{(2\,\pm2)}(x) &= \pm\frac{1}{2}\left[j'_\ell(x) + 2\frac{j_\ell(x)}{x}\right]
\end{aligned}
$$

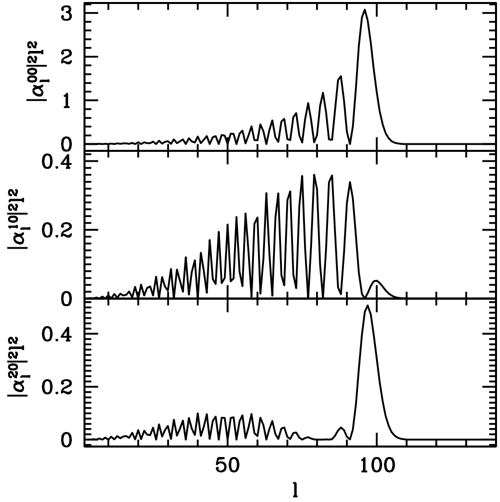

The functions $\ell^2|\alpha_\ell^{(00)}|^2$ (top), $\ell^2|\alpha_\ell^{(10)}|^2$ (middle) and $\ell^2|\alpha_\ell^{(20)}|^2$ (bottom) are shown as function of ℓ for fixed $x = 100$. These are the kernels relevant for the scalar temperature anisotropies. Their amplitude and shape will determine how strongly the corresponding source terms in the Boltzmann eqn. influence the final anisotropy spectrum.

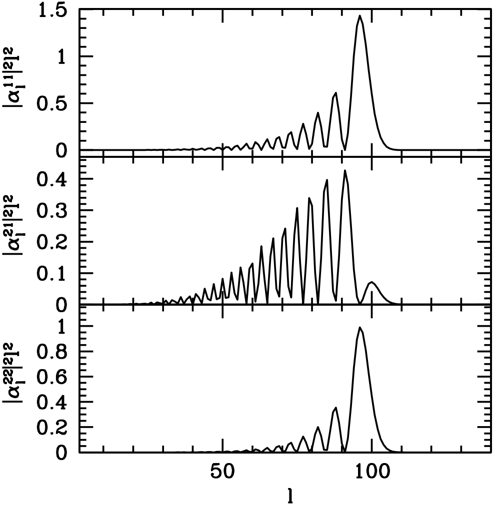

The functions $\ell^2|\alpha_\ell^{(11)}|^2$ (top), $\ell^2|\alpha_\ell^{(21)}|^2$ (middle) and $\ell^2|\alpha_\ell^{(22)}|^2$ (bottom) are shown as function of ℓ for fixed $x = 100$. These are the kernels relevant for vector, $\alpha_\ell^{(11)}$ and $\alpha_\ell^{(21)}$, and tensor, $\alpha_\ell^{(22)}$, temperature anisotropies.

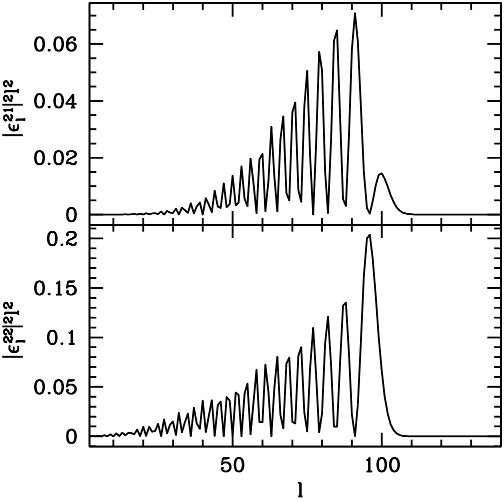

The functions $\ell^2|\epsilon_\ell^{(21)}|^2$ (top) and $\ell^2|\epsilon_\ell^{(22)}|^2$ (bottom) are shown as function of ℓ for fixed $x = 100$. These are the kernels relevant for *E*–polarization of vector and tensor modes respectively. Since $\ell^2|\epsilon_\ell^{(20)}|^2 = \ell^2|\alpha_\ell^{(22)}|^2$ this kernel for scalar *E*–polarization is not re-plotted. Note that the vector *E*–polarization kernel is very small and the scalar kernel is still about a factor of 5 larger than the tensor kernel.

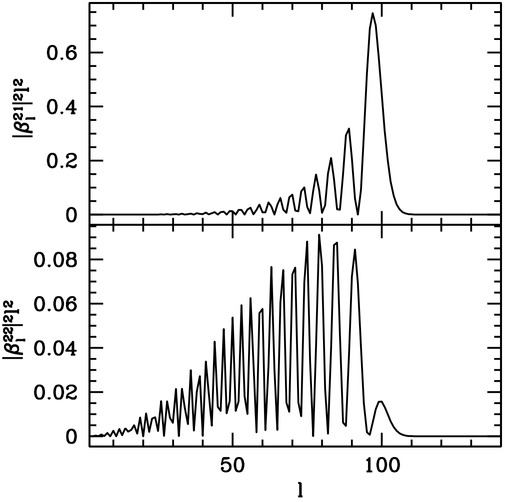

The functions $\ell^2|\beta_\ell^{(21)}|^2$ (top) and $\ell^2|\beta_\ell^{(22)}|^2$ (bottom) are shown as function of ℓ for fixed $x = 100$. These are the kernels relevant for B–polarization of vector and tensor modes respectively. Note that the vector B–polarization kernel is much larger than the tensor one. This is the opposite of what we found for E-polarization.

$$\dot{\mathcal{M}}_\ell^{(m)} + k\left[\frac{\sqrt{(\ell+1)^2-m^2}}{(2\ell+3)}\mathcal{M}_{\ell+1}^{(m)} - \frac{\sqrt{\ell^2-m^2}}{(2\ell+1)}\mathcal{M}_{\ell-1}^{(m)}\right] = S_\ell^{(m)} + \dot\kappa[P_\ell^{(m)} - \mathcal{M}_\ell^{(m)}]$$

with

$$\begin{aligned}
S_\ell^{(0)} &= -\delta_{\ell 1}k(\Psi+\Phi)\\
S_\ell^{(\pm1)} &= -\delta_{\ell 2}\frac{i}{\sqrt{3}}k\sigma_\pm\\
S_\ell^{(\pm2)} &= \delta_{\ell 2}\frac{1}{\sqrt{3}}k\dot{H}_{\pm2}\\
P_\ell^{(0)} &= \delta_{\ell 0}\mathcal{M}_0^{(0)} + V_b^{(0)}\delta_{\ell 1} + \delta_{\ell 2}\frac{1}{10}[\mathcal{M}_2^{(0)} - \sqrt{6}\mathcal{E}_2^{(0)}]\\
P_\ell^{(\pm1)} &= V_b^{(\pm1)}\delta_{\ell 1} + \delta_{\ell 2}\frac{1}{10}[\mathcal{M}_2^{(\pm1)} - \sqrt{6}\mathcal{E}_2^{(\pm1)}]\\
P_\ell^{(\pm2)} &= \delta_{\ell 2}\frac{1}{10}[\mathcal{M}_2^{(\pm2)} - \sqrt{6}\mathcal{E}_2^{(\pm2)}]
\end{aligned}$$

$$\dot{\mathcal{E}}_\ell^{(m)} + k\left[\frac{\sqrt{[(\ell+1)^2-4][(\ell+1)^2-m^2]}}{(2\ell+1)(2\ell+3)}\mathcal{E}_{\ell+1}^{(m)} - \frac{2m}{\ell(\ell+1)}\mathcal{B}_\ell^{(m)} - \frac{\sqrt{(\ell^2-4)(\ell^2-m^2)}}{(2\ell+1)(2\ell+3)}\mathcal{E}_{\ell-1}^{(m)}\right] = -\dot\kappa[\mathcal{E}_\ell^{(m)} + \sqrt{6}P_\ell^{(m)}]$$

$$\dot{\mathcal{B}}_\ell^{(m)} + k\left[\frac{\sqrt{[(\ell+1)^2-4][(\ell+1)^2-m^2]}}{(2\ell+1)(2\ell+3)}\mathcal{B}_{\ell+1}^{(m)} + \frac{2m}{\ell(\ell+1)}E_\ell^{(m)} - \frac{\sqrt{(\ell^2-4)(\ell^2-m^2)}}{(2\ell+1)(2\ell+3)}\mathcal{B}_{\ell-1}^{(m)}\right] = -\dot\kappa\mathcal{B}_\ell^{(m)}$$

$$
\begin{aligned}
\frac{\mathcal{M}_\ell^{(0)}(t_0)}{2\ell+1} &= \int_{t_{\rm in}}^{t_0} dt e^{-\kappa(t_0,t)}\Big[ik(\Psi+\Phi+\dot\kappa V^{(b)})\alpha_\ell^{(10)}(x) \\
&\quad +\dot\kappa\left(\mathcal{M}_0^{(0)}\alpha_\ell^{(00)}(x)+\frac{1}{10}[\mathcal{M}_2^{(0)}-\sqrt{6}E_2^{(0)}]\alpha_\ell^{(20)}(x)\right)\Big] \\
\frac{\mathcal{M}_\ell^{(\pm1)}(t_0)}{2\ell+1} &= \int_{t_{\rm in}}^{t_0} dt e^{-\kappa(t_0,t)}\left[-\frac{ik}{\sqrt{3}}\sigma_\pm\alpha_\ell^{(2\ \pm1)}(x)+\dot\kappa V_\pm^{(b)})\alpha_\ell^{(1\ \pm1)}(x)\right. \\
&\quad \left.+\frac{\dot\kappa}{10}[\mathcal{M}_2^{(\pm1)}-\sqrt{6}E_2^{(\pm1)}]\alpha_\ell^{(2\ \pm1)}(x)\right] \\
\frac{\mathcal{M}_\ell^{(\pm2)}(t_0)}{2\ell+1} &= \int_{t_{\rm in}}^{t_0} dt e^{-\kappa(t_0,t)}\left[\frac{1}{\sqrt{3}}k\dot H_{\pm2}+\frac{\dot\kappa}{10}[\mathcal{M}_2^{(\pm2)}-\sqrt{6}\mathcal{E}_2^{(\pm2)}]\right]\alpha_\ell^{2\ \pm2}(x) \\
\frac{\mathcal{E}_\ell^{(m)}(t_0,\mathbf{n})}{2\ell+1} &= -\sqrt{6}\int_{t_{\rm in}}^{t_0} dt e^{-\kappa(t_0,t)}\frac{\dot\kappa}{10}(\mathcal{M}_2^{(m)}-\sqrt{6}\mathcal{E}_2^{(m)})\epsilon_\ell^{(2m)}(x) \\
\frac{\mathcal{B}_\ell^{(m)}(t_0,\mathbf{n})}{2\ell+1} &= -\sqrt{6}\int_{t_{\rm in}}^{t_0} dt e^{-\kappa(t_0,t)}\frac{\dot\kappa}{10}(\mathcal{M}_2^{(m)}-\sqrt{6}\mathcal{E}_2^{(m)})\beta_\ell^{(2m)}(x)
\end{aligned}
\tag{1}
$$

Spectra (5)

$$\begin{aligned}
\langle \mathcal{M}_\ell^{(s)}(\mathbf{k})\mathcal{M}_\ell^{(s)*}(\mathbf{k}')\rangle &\equiv (2\pi)^3\delta^3(\mathbf{k}-\mathbf{k}')M_\ell^{(s)}(k) \\
\langle \mathcal{E}_\ell^{(s)}(\mathbf{k})\mathcal{E}_\ell^{(s)*}(\mathbf{k}')\rangle &\equiv (2\pi)^3\delta^3(\mathbf{k}-\mathbf{k}')E_\ell^{(s)}(k) \\
\langle \mathcal{B}_\ell^{(s)}(\mathbf{k})\mathcal{B}_\ell^{(s)*}(\mathbf{k}')\rangle &\equiv (2\pi)^3\delta^3(\mathbf{k}-\mathbf{k}')B_\ell^{(s)}(k) \\
\langle \mathcal{E}_\ell^{(s)}(\mathbf{k})\mathcal{M}_\ell^{(s)*}(\mathbf{k}')\rangle &\equiv (2\pi)^3\delta^3(\mathbf{k}-\mathbf{k}')F_\ell^{(s)}(k)
\end{aligned}$$

$$\begin{aligned}
(2\ell+1)^2 C_\ell^{(\mathcal{M})} &\equiv (2\ell+1)^2\langle |a_{\ell m}|^2\rangle = \frac{2}{\pi}\sum_{s=-2}^{2}\int dk k^2 M_\ell^{(s)}(k) \\
(2\ell+1)^2 C_\ell^{(\mathcal{E})} &\equiv (2\ell+1)^2\langle |e_{\ell m}|^2\rangle = \frac{2}{\pi}\sum_{s=-2}^{2}\int dk k^2 E_\ell^{(s)}(k) \\
(2\ell+1)^2 C_\ell^{(\mathcal{B})} &\equiv (2\ell+1)^2\langle |b_{\ell m}|^2\rangle = \frac{2}{\pi}\sum_{s=-2}^{2}\int dk k^2 B_\ell^{(s)}(k) \\
(2\ell+1)^2 C_\ell^{(\mathcal{M}\mathcal{E})} &\equiv (2\ell+1)^2\langle a_{\ell m}^* e_{\ell m}\rangle = \frac{2}{\pi}\sum_{s=-2}^{2}\int dk k^2 F_\ell^{(s)}(k)
\end{aligned}$$

Spectra: WMAP data (7 year)

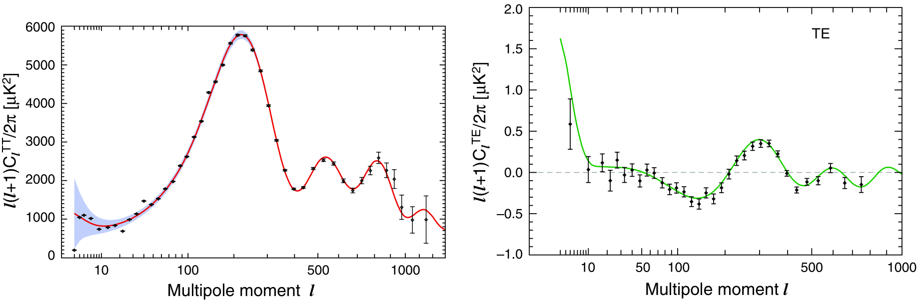

Spectra: Atacama Cosmology Telescope data (2011)

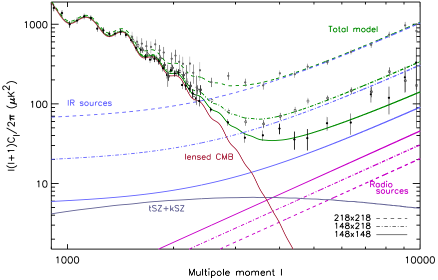

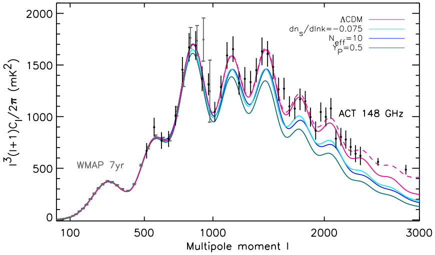

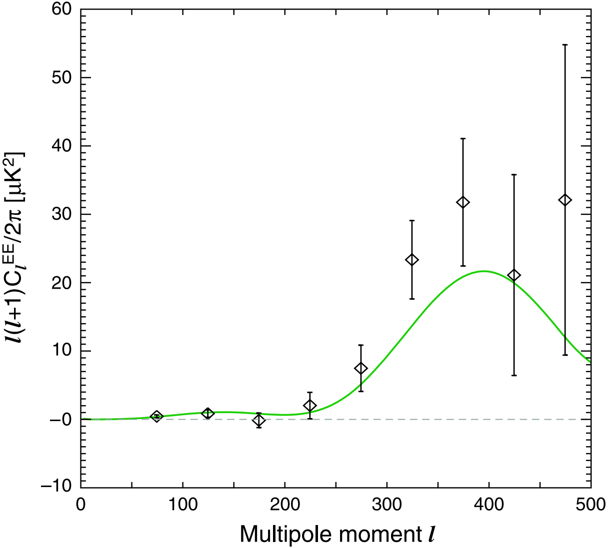

WMAP 7 year, Larson et al. 2009

The CMB polarization spectrum

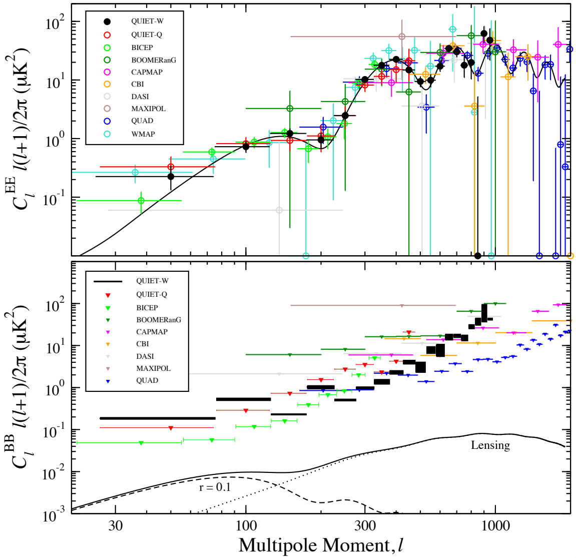

QUIET (2012)

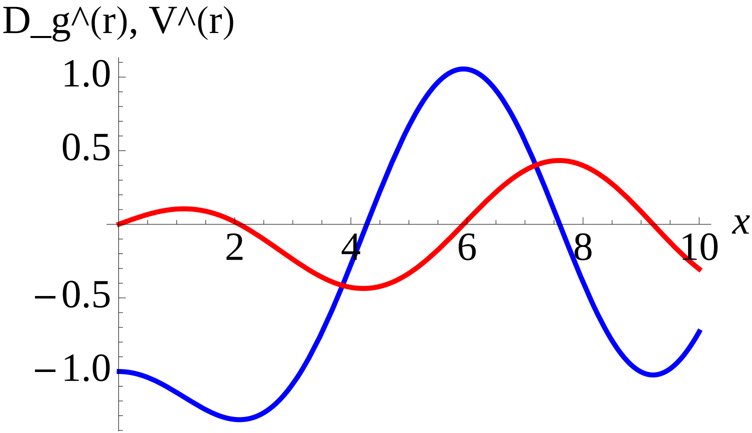

$D_g^{(r)}(x)$ (blue) and $V^{(r)}$ (red)

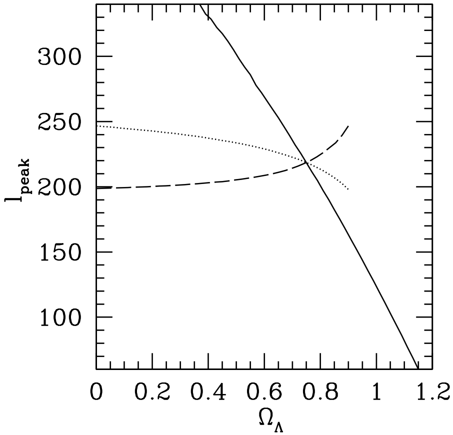

The position of the first peak as function of Ω_Λ. In the solid line we vary Ω_K, leaving all other parameters fixed, for the dashed line we vary Ω_m and Ω_Λ keeping $K = 0$ fixed. For the dotted line we vary Ω_Λ and Ω_m again with $K = 0$ at fixed $\Omega_m h^2$. The fixed parameters are $\Omega_K = 0$, $h = 0.72$, $\Omega_b h^2 = 0.022$, $\Omega_m = 0.25$, $n_s = 0.96$, $\tau_{ri} = 0.085$. Therefore, all the curves cross at $\Omega_\Lambda = 0.75$.

Acoustic peaks

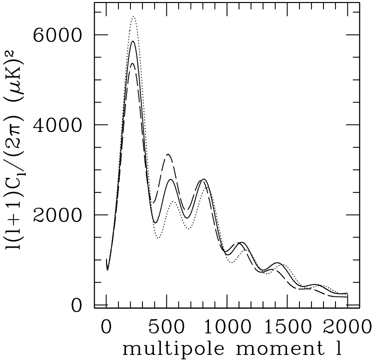

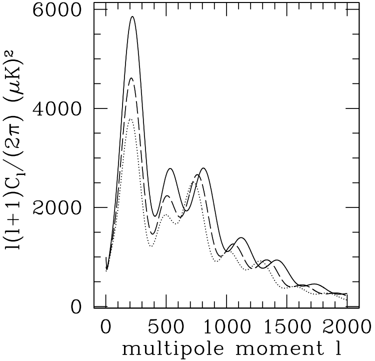

Left: the asymmetry of even and odd peaks and its dependence on $\Omega_b h^2$. $\Omega_b h^2 = 0.02$ (solid line), $\Omega_b h^2 = 0.03$ (dotted) and $\Omega_b h^2 = 0.01$ (dashed).
Right: $\Omega_b h^2 = 0.02$ is fixed and three different values for the matter density are chosen, $\Omega_m h^2 = 0.12$ (solid), $\Omega_m h^2 = 0.2$ (dashed) $\Omega_m h^2 = 0.3$ (dotted). A smaller value of $\Omega_m h^2$ boosts the height especially of the first peak due to the early integrates Sachs-Wolfe effect. The peaks are also somewhat shifted since D_A depends on Ω_m.

Parameters

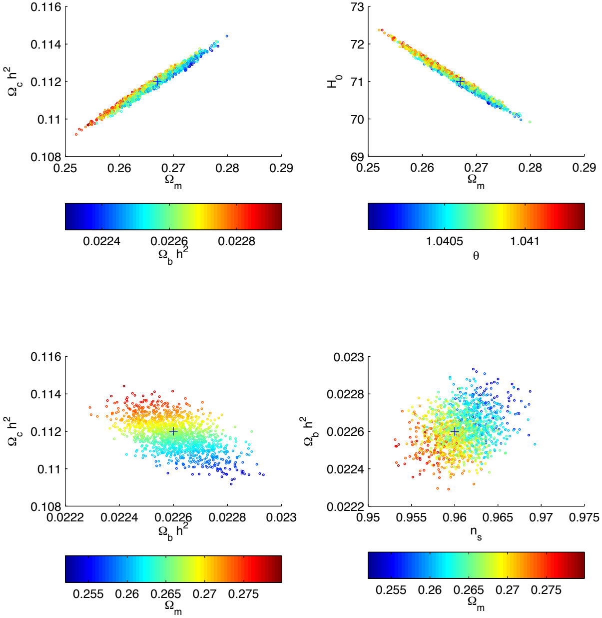

(Howlett et al. 2012)

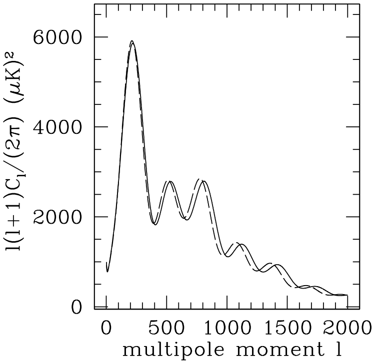

Massless neutrinos(solid) and neutrinos with mass $m_\nu = 2$eV (dashed lines). In the left hand panel $\Omega_{cdm}h^2 = 0.12$ is fixed while on the right hand side $\Omega_m h^2 = 0.144$ is fixed. In all curves $\Omega_{\rm tot} = 1$, $\Omega_b h^2 = 0.022$ and $h = 0.7$. Keeping $\Omega_m h^2$ fixed, adding neutrinos acts a bit like a lower matter density, since the neutrinos are not yet fully non-relativistic at decoupling.

Cosmological parameters

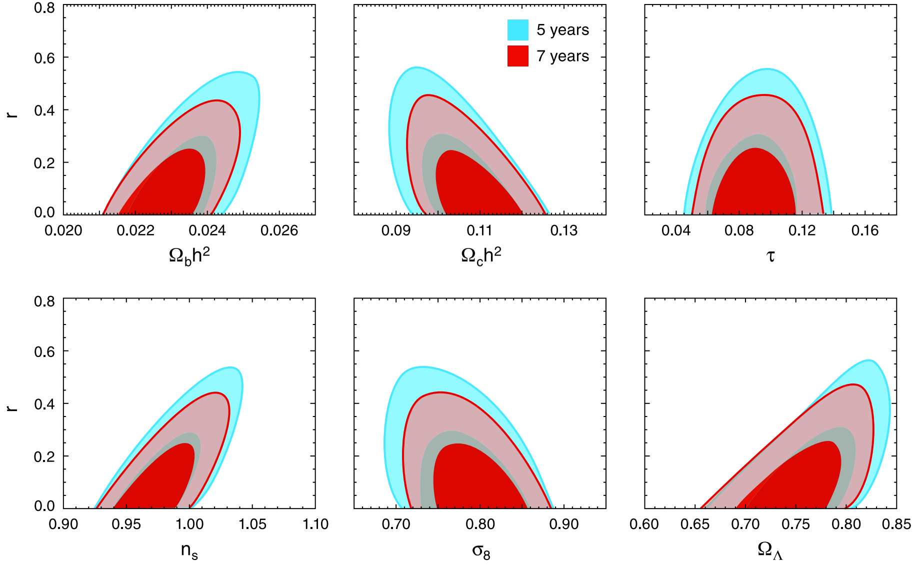

WMAP 7 year, Larson et al. 2009

Cosmological parameters

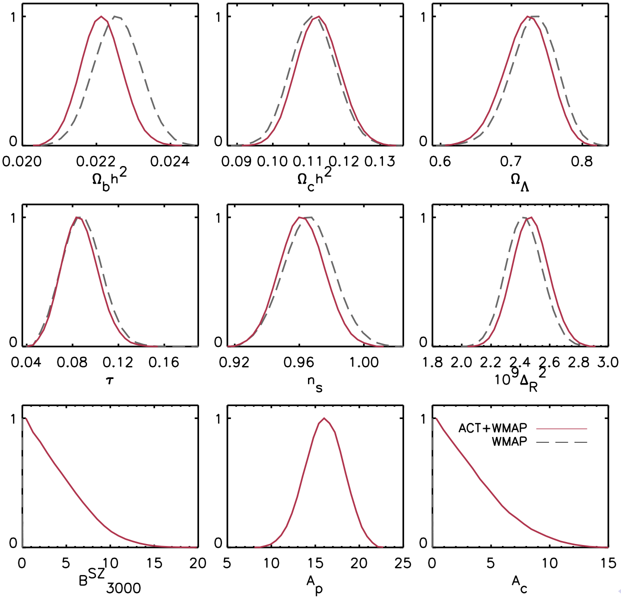

WMAP 7 year and ACT data

J. Dunkley et al. 2010

$\mathcal{B}^{SZ}_{3000}$ = themal SZ power at $\ell = 3000$

A_p = Poisson noise in IR sources at $\ell = 3000$

A_c = clustered IR sources at $\ell = 3000$

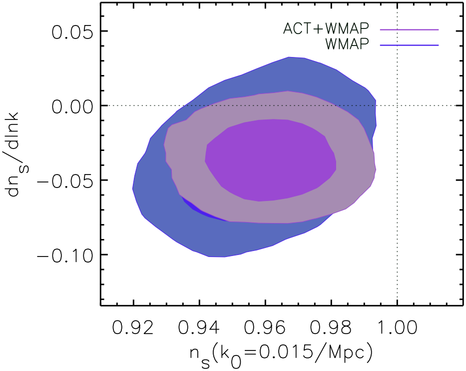

2D marginalized limits (68% and 95% CL) for n_s, plotted at the pivot point $k_0 = 0.015/\mathrm{Mpc}$, and the running of the index $dn_s/d\ln k$, for ACT+WMAP, compared to WMAP. This model has no tensor fluctuations. A negative running is preferred, but the data are consistent with a power-law spectral index, with $dn_s/d\ln k = 0$.

J. Dunkley et al. 2010.

Cosmological parameters

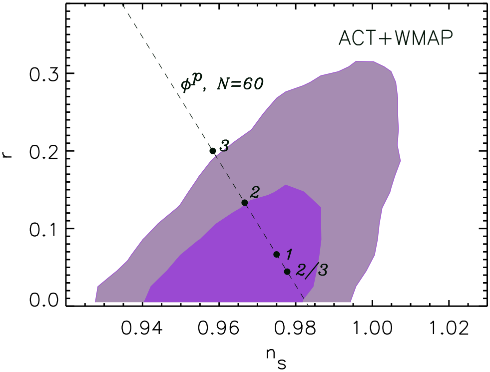

2D marginalized limits (68% and 95% CL) for the tensor-to-scalar ratio r, and the scalar spectral index n_s, for ACT+WMAP data. By measuring the $\ell > 1000$ spectrum, the longer lever arm from ACT data further breaks the n_s - r degeneracy, giving a marginalized limit $r < 0.25$ (95% CL) from the CMB alone. The predicted values for a chaotic inflationary model with inflaton potential $V(\phi) \propto \phi^p$ with 60 e-folds are shown for $p = 3, 2, 1, 2/3$; $p > 3$ is disfavored at $>$ 95% CL.
J. Dunkley et al. 2010.

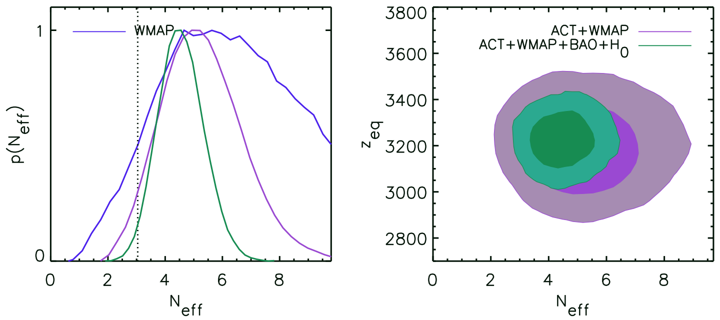

Constraints on the effective number of relativistic species, $N_{\rm eff}$. Left: One-dimensional marginalized distribution for $N_{\rm eff}$, for data combinations indicated in the right panel. (Standard model: $N_{\rm eff} = 3.04$, dotted line). Right: 2D marginalized distribution for $N_{\rm eff}$and equality redshift $z_{\rm eq}$, showing that $N_{\rm eff}$ can be measured separately from zeq. $N_{\rm eff}$ is bounded from above and below by combining the small-scale ACT measurements of the acoustic peaks with WMAP measurements. The limit is tightened by adding BAO and H_0 constraints, breaking the degeneracy between $N_{\rm eff}$ and the matter density by measuring the expansion rate at late times.

J. Dunkley et al. 2010. $N_{\rm eff} = 5.3 \pm 1.3$ (CMB alone).

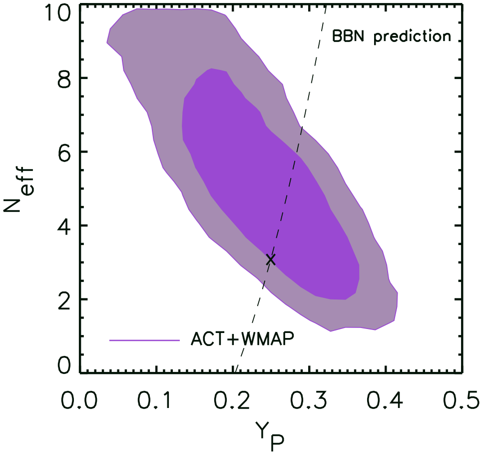

2D marginalized limits (68% and 95% CL) for the primordial helium mass fraction Y_P and the number of relativistic species $N_{\rm eff}$. The two are partly degenerate, as increasing $N_{\rm eff}$ or Y_P leads to increased damping of the power spectrum. The predicted standard-BBN relation between $N_{\rm eff}$ and Y_P is indicated. The concordance $N_{\rm eff} = 3.04$, $Y_P = 0.25$ model lies on the edge of the two-dimensional 68% CL, and a model with $N_{\rm eff} = 0$, $Y_P = 0$ is excluded at high significance.
J. Dunkley et al. 2010.

Cosmological parameters

ΛCDM and extended model parameters and 68% confidence intervals from the ACT 2008 data combined with seven-year WMAP data.

Parameter[a]	ΛCDM	ΛCDM $+ dn_s/d\ln k$	ΛCDM $+ r$	ΛCDM $+ N_{\rm eff}$	ΛCDM $+ Y_P$	ΛCDM $+ G\mu$
$100\Omega_b h^2$	2.214 ± 0.050	2.167 ± 0.054	2.246 ± 0.057	2.252 ± 0.055	2.236 ± 0.052	2.240 ± 0.053
$\Omega_c h^2$	0.1127 ± 0.0054	0.1214 ± 0.0074	0.1099 ± 0.0058	0.152 ± 0.025	0.1166 ± 0.0061	0.1115 ± 0.0055
Ω_Λ	0.721 ± 0.030	0.670 ± 0.046	0.738 ± 0.030	0.720 ± 0.030	0.711 ± 0.031	0.730 ± 0.029
n_s	0.962 ± 0.013	1.032 ± 0.039	0.974 ± 0.016	0.993 ± 0.021	0.974 ± 0.015	0.963 ± 0.013
τ	0.087 ± 0.014	0.092 ± 0.016	0.087 ± 0.015	0.089 ± 0.015	0.087 ± 0.015	0.087 ± 0.015
$10^9 \Delta^2_{\mathcal{R}}$	2.47 ± 0.11	2.44 ± 0.11	2.37 ± 0.13	2.40 ± 0.12	2.45 ± 0.11	2.43 ± 0.11
$dn_s/d\ln k$	0	-0.034 ± 0.018	0	0	0	0
r	0	0	< 0.25	0	0	0
$N_{\rm eff}$	3.04	3.04	3.04	5.3 ± 1.3	3.04	3.04
Y_P	0.25	0.25	0.25	0.25	0.313 ± 0.044	0.25
$G\mu$	0	0	0	0	0	$< 1.6 \times 10^{-7}$
σ_8	0.813 ± 0.028	0.841 ± 0.032	0.803 ± 0.030	0.906 ± 0.059	0.846 ± 0.035	0.803 ± 0.029
Ω_m	0.279 ± 0.030	0.330 ± 0.046	0.262 ± 0.030	0.280 ± 0.030	0.289 ± 0.031	0.270 ± 0.029
H_0	69.7 ± 2.5	66.1 ± 3.0	71.4 ± 2.8	78.9 ± 5.9	69.5 ± 2.3	70.6 ± 2.5
$B^{\rm SZ}_{3000}$ $(\mu{\rm K}^2)$	< 10.2	< 12.3	< 10.0	< 12.1	< 13.0	< 8.8
A_p $(\mu{\rm K}^2)$	16.0 ± 2.0	14.9 ± 2.2	16.0 ± 2.0	15.1 ± 2.1	15.0 ± 2.1	16.1 ± 1.9
A_c $(\mu{\rm K}^2)$	< 8.7	< 10.4	< 8.0	< 11.1	< 11.2	< 7.4
$-2\ln\mathcal{L}$	7500.0	7498.1	7500.1	7498.7	7498.8	7500.1

(a) For one-tailed distributions, the upper 95% CL is given. For two-tailed distributions the 68% CL are shown. J. Dunkley et al. 2010.

Degeneracy

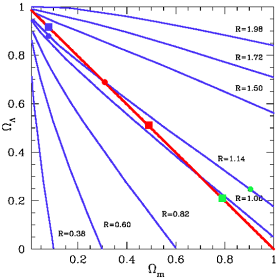

On left lines of equal angular diameter distance are indicated. $R = D_A/D_A(\Omega_\Lambda = 0.7, Om_m = 0.3, h = 0.7)$. Below on the left: $\Omega_K > 0$ (dashed), $\Omega_K < 0$ (dotted) and $\Omega_K = 0$ (solid), with fixed D_A, $\Omega_m h^2$, $\Omega_b h^2$. On the right: three spectra with $K = 0$, fixed $\Omega_m h^2$, $\Omega_b h^2$, but different D_A (the squares indicated in the top panel on the $K = 0$ line).

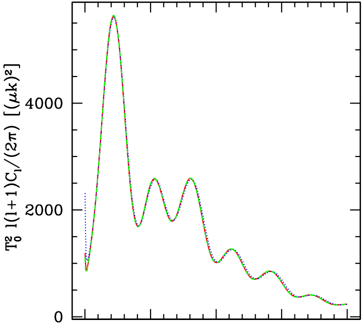

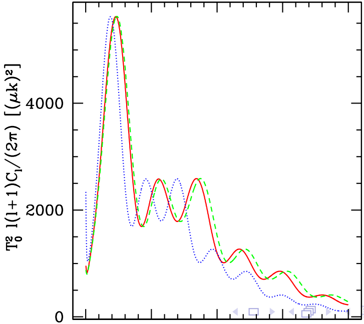

Degeneracy

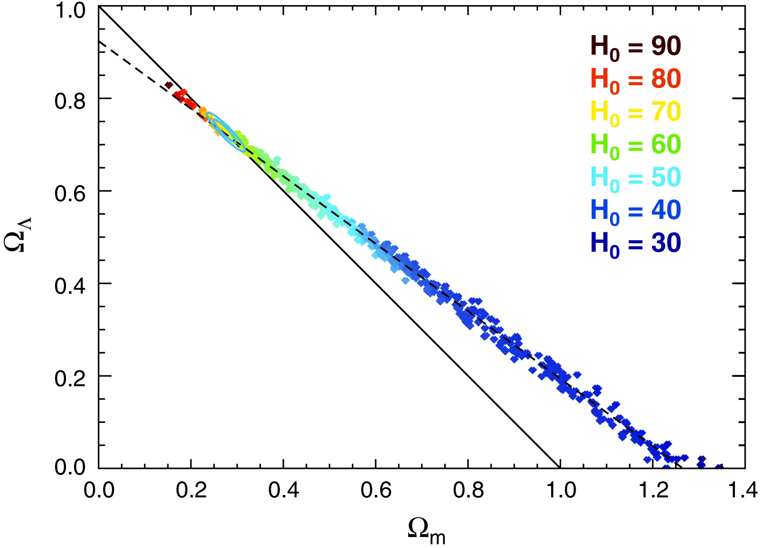

WMAP 7 year, Larson et al. 2009

Degeneracy

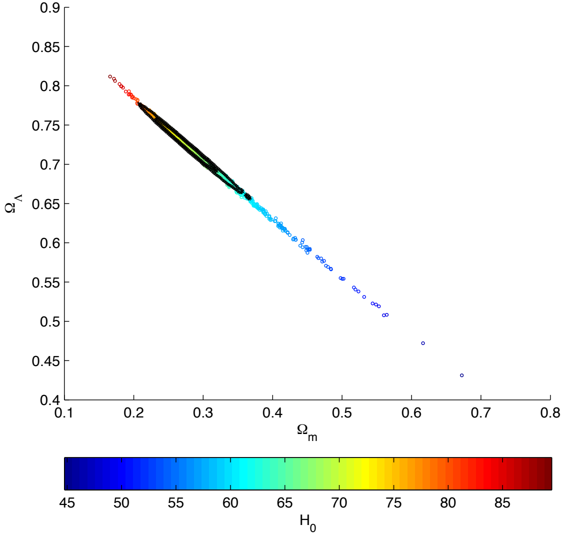

Lifting the degeneracy with CMB lensing
(Planck forecast).
(Howlett et al. 2012)

Degeneracy

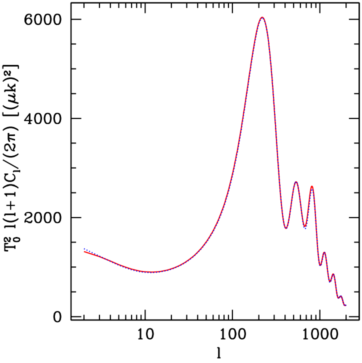

A spectrum of purely scalar perturbations with $n_s = 0.96$ (solid) is compared to one with a tensor contribution of $r = 0.3$ (dotted). The cosmological parameters of the two models differ somewhat but are all within 2 sigma of the 'concordance values':

Scalar model:

$(h = 0.73,\ \Omega_b h^2 = 0.0225,$
$\Omega_m h^2 = 0.135,\ \tau = 0.1, n_s = 0.96)$

Model with tensors, $r = 0.3$**:**

$(h = 0.8,\ \Omega_b h^2 = 0.023,$
$\Omega_m h^2 = 0.118, \tau = 0.1, n_s = 1.0, n_T = 0)$

These two models cannot be distinguished from their temperature anisotropies.

Conclusions and outlook

- The CMB anisotropies and polarization are a superb cosmological tool.

Conclusions and outlook

- The CMB anisotropies and polarization are a superb cosmological tool.
- Their theory is simple (to a big extent linear) physics and we can compute them to high accuracy.

- The CMB anisotropies and polarization are a superb cosmological tool.
- Their theory is simple (to a big extent linear) physics and we can compute them to high accuracy.
- Their precision measurements have revolutionized cosmology from an 'order magnitude' to 'precision' science.

Conclusions and outlook

- The CMB anisotropies and polarization are a superb cosmological tool.
- Their theory is simple (to a big extent linear) physics and we can compute them to high accuracy.
- Their precision measurements have revolutionized cosmology from an 'order magnitude' to 'precision' science.
- They provide a unique window to the very high energy physics of inflation.

Conclusions and outlook

- The CMB anisotropies and polarization are a superb cosmological tool.
- Their theory is simple (to a big extent linear) physics and we can compute them to high accuracy.
- Their precision measurements have revolutionized cosmology from an 'order magnitude' to 'precision' science.
- They provide a unique window to the very high energy physics of inflation.
- And there is more to come... New data from
  Planck, QUIET, CG, KUPID, EBEX, COSMOSOMAS, QUIJOTE...
  may discover

- The CMB anisotropies and polarization are a superb cosmological tool.
- Their theory is simple (to a big extent linear) physics and we can compute them to high accuracy.
- Their precision measurements have revolutionized cosmology from an 'order magnitude' to 'precision' science.
- They provide a unique window to the very high energy physics of inflation.
- And there is more to come... New data from
  Planck, QUIET, CG, KUPID, EBEX, COSMOSOMAS, QUIJOTE...
  may discover
  - B-polarization $\Rightarrow$ gravitational waves from inflation.
  - Additional 'neutrino' species.
  - Sources like topological defects, primordial magnetic fields...
  - Other unexpected events of the early Universe.

Stay tuned!